Interdependencies between the Evolution of Amorphous and Crystalline Regions during Isothermal Cold Crystallization of Poly(ether−ether−ketone)

Dimitri A. Ivanov,*,† Roger Legras, and Alain M. Jonas

Unité de physique et de chimie des hauts polymères, Université catholique de Louvain,
Place Croix du Sud, 1, 1348 Louvain-la-Neuve, Belgium

Received August 3, 1998; Revised Manuscript Received December 17, 1998

ABSTRACT: We have studied the isothermal cold crystallization of poly(ether−ether−ketone) (PEEK) by atomic force microscopy, densitometry, differential scanning calorimetry (DSC), dynamic mechanical analysis (DMA), and small- and wide-angle X-ray scattering (SAXS and WAXS). A two-stage process was clearly evidenced. The first stage results in the progressive consumption of free amorphous regions by growing spherulites. Lamellae grow in tightly packed bundles, with no evidence for a random insertion mechanism. DSC and DMA consistently show the progressive disappearance of the α_1 relaxation typical of the initially amorphous PEEK. Simultaneously, a new relaxation appears a few degrees higher (α_2 relaxation) and develops at the expense of α_1 relaxation. It corresponds to the formation of amorphous regions constrained by neighboring crystals. On the basis of a simple simulation, we show that the experimental data in this second stage of crystallization can be accounted for by a simple stack thickening process in which new lamellae are progressively added in parallel to previously formed lamellar stacks.

Introduction

A unique characteristic of semicrystalline polymers is the coexistence of amorphous and crystalline regions in the material.[1,2] Initially, attention was essentially directed to crystalline regions, as they are more amenable to characterization. Progressively, interest extended to crystal/amorphous boundaries, the so-called crystal/amorphous interphases.[3,4] However, the knowledge of the structure of amorphous regions in semicrystalline polymers remains scarce. Conformational changes have been detected experimentally in the amorphous regions at the vicinity of crystallite surfaces.[5,6] Some theoretical models[7−10] have attempted to predict the morphological characteristics of semicrystalline polymers, taking into account energy terms due to the perturbations of the chain conformations in spatially confined amorphous regions nearby crystal boundaries. Such perturbations are expected to increase with increasing stiffness of the chains and the resulting inability of the chains to form regular folds with adjacent reentry.[11] In this case, the physical interconnection of crystalline and amorphous regions via the tethering of amorphous segments to the crystallite surfaces is an important property to take into account.

For semirigid para-linked aromatic polymers such as poly(ether−ether−ketone) (PEEK, poly(oxy-1,4-phenyleneoxy-1,4-phenylenecarbonyl-1,4-phenylene)) or poly(ethylene terephthalate) (PET), there are indications in the literature that the interactions between amorphous and crystalline regions are strong.[12−16] The presence of crystalline regions impacts dramatically the glass transition temperature (T_g),[12,15,16] the glass[16,17−20] and subglass[15,21,22] relaxation characteristics of amorphous regions, and the ability of amorphous regions to undergo physical aging.[13] In this case, a majority of amorphous regions in the semicrystalline structure become perturbed, or constrained, upon crystallization. This modification of amorphous regions has been tentatively described in terms of a three-phase model containing a so-called “rigid amorphous phase”.[16,23] Interestingly, a reverse influence of amorphous regions on crystals can also be observed for these polymers. Some properties of crystalline regions, such as crystal thermal expansion, are clearly influenced by properties of amorphous regions.[14]

Such polymers appear thus well-suited to examine how the structural modification of amorphous regions in the course of crystallization affects the crystallization process itself. Indeed, the progressive constraining of amorphous regions during crystallization should limit the attainable degree of crystallinity and may explain the formation of imperfect crystalline structures. This may in turn account for the failure of simple one-stage phenomenological models such as Avrami's[24] to describe the overall cold crystallization kinetics of these polymers.[25−29]

Given these observations, we have undertaken research focusing on the interactions between amorphous and crystalline regions in PEEK. (Abstracts of this work have been published in refs 30 and 31.) In a previous paper, we have concentrated on vitrification effects on the crystallization kinetics of PEEK and PEEK/poly(ether−imide) blends.[32] In the present paper, we intend to correlate the evolutions of amorphous and crystalline regions during isothermal crystallization of PEEK from the glass at very low temperatures ($\sim T_g + 10$ °C). While X-ray scattering, densitometry, and atomic force microscopy (AFM) will be used to follow the crystal growth and morphology, simultaneous studies by dynamic mechanical analysis and differential scanning calorimetry will assess the relaxation properties of amorphous regions. These relaxation data will be used to obtain complementary information about the mechanisms of different stages of crystallization.

---

* To whom correspondence should be addressed. E-mail: divanov@ulb.ac.be; URL: http://www.ulb.ac.be/sciences/polphy/.

† Present address: Laboratoire de Physique des Polymères, CP 223, Université Libre de Bruxelles, Boulevard du Triomphe, 1050 Bruxelles, Belgium.

10.1021/ma981220o CCC: $18.00

Experimental Section

Sample Preparation. Quenched amorphous PEEK sheets (350−500 μm thick) were prepared from dry commercial powder (I.C.I. grade 150P) as described elsewhere.[14] Thin solution cast films of PEEK on mica were prepared as described in ref 33.

Dynamic mechanical analysis (DMA) was performed in tension mode in a Rheometrics RSAII on rectangular 5 × 30 mm^2 specimens. The isothermal crystallization was performed directly in the DMA oven at $T_c = 156$ °C. Temperature was measured with a thermocouple positioned close to the sample; the temperature stability was about 0.2 °C. Most measurements were performed on one single sample annealed at 156 °C. After certain times (t_c) the crystallization was stopped by rapid cooling, and the sample was afterward immediately rescanned in the DMA at 1.0 °C/min (test frequency 1.0 Hz; dynamic deformation 0.02%) up to 156 °C. For the longest crystallization times, however, a new sample was used for each experiment and scanned up to 160−168 °C after crystallization in the DMA depending upon the sample's glass transition temperature (T_g). DMA T_g of the starting amorphous sheets, defined as the temperature corresponding to the maximum of the dynamical mechanical loss modulus, was 143 °C.

Differential scanning calorimetry (DSC) measurements were performed in a TA 2920 apparatus under He atmosphere. The DSC was calibrated with indium and zinc. Samples of amorphous PEEK (10−15 mg) were prepared in the form of flat disks. A typical DSC program included an isothermal treatment at $T_c = 156$ °C for different t_c's, rapid cooling, followed by a final temperature ramp at 10 °C/min. The enthalpies of cold crystallization were calculated using an iterative integral baseline reconstruction procedure described elsewhere.[34] The calorimetric T_g was defined as the temperature corresponding to half-devitrification as determined on the heat capacity curve. Due to slight differences in the absolute temperature calibrations of the DSC and DMA furnaces, the kinetic data obtained by these two techniques cannot be compared directly.

For all other experiments described below, a single set of samples was prepared by crystallizing 10 amorphous PEEK sheets for different times in the DMA oven.

Densitometry measurements were carried out in a density gradient column (water/NaBr), with an accuracy better than 2×10^{-4} g cm^{-3}. The volume crystallinity was evaluated from a two-phase model, based on estimations[35] for the specific weights of crystal ($\rho_c = 1.394$ g cm^{-3}) and pure amorphous PEEK ($\rho_a = 1.264$ g cm^{-3}).

Small-angle X-ray scattering (SAXS) experiments were performed in an evacuated Kratky compact camera mounted on a Siemens rotating anode generator (Ni-filtered Cu Kα radiation, 40 kV/300 mA). A position-sensitive proportional counter (PSPC, Braun) was used to record the diffraction patterns. The data were first corrected for absorption, parasitic scattering, and detector dead time. In a second stage, the data were fitted to the sum of Porod's law and Ruland's function representing the fluidlike background scattering[36] in the large s range (0.05−0.1 Å^{-1}):

$$\tilde{I}(s) = \tilde{I}_{\mathrm{Porod}}(s) + A_F \exp(Bs^2) \qquad (1)$$

with $s = 2\sin(\theta)/\lambda$ where θ is half the angle between incident and scattered beams and λ the X-ray wavelength. In eq 1, $\tilde{I}(s)$ stands for the measured (smeared) intensity, A_F and B are constants, and $\tilde{I}_{\mathrm{Porod}}(\boldsymbol{s})$ is a generalized smeared Porod's law taking into account the presence of sigmoidal-gradient density transition layers at crystal boundaries. For our experimental setup, the X-ray beam profile measured in the detector plane was found to be adequately described in its longer dimension by a Gaussian of standard deviation $\sigma_{\mathrm{beam}} = 0.66$ cm. We thus consistently used the expression of $\tilde{I}_{\mathrm{Porod}}(s)$ given by Koberstein et al.:[37]

$$\tilde{I}_{\mathrm{Porod}}(s) = \frac{K'}{s^3}\exp(p^2s^2)[(1 - 8\pi^2\alpha^2s^2)\,\mathrm{erfc}(2\pi\alpha s) + 4\sqrt{\pi}\alpha s\exp(-4\pi^2\alpha^2s^2)] \qquad (2)$$

where

$$\alpha = [\sigma^2 + (p/2\pi)^2]^{1/2} \qquad (3)$$

and

$$K' = \left(\frac{\pi}{2}\right) W_1(0) K_p \qquad (4)$$

In eqs 2−4 σ represents the root-mean-square (RMS) thickness of the density transition layers and K_p is Porod's constant. The parameter p is related to the standard deviation of the beam profile, sample-to-detector distance (SDD), and the X-ray wavelength:

$$p = \lambda \mathrm{SDD}/(\sqrt{2}\sigma_{\mathrm{beam}}) \qquad (5)$$

This parameter allows to describe the beam shape in reciprocal space units as

$$W_1(s) = W_1(0)\exp(-p^2s^2) \qquad (6)$$

The fluidlike background scattering was subtracted from $\tilde{I}(s)$, and these curves were then desmeared using a variant of Glatter's algorithm,[38] taking into account the actual profile of the incident beam. The one-dimensional correlation function was obtained by Fourier transformation of the Lorentz-corrected desmeared intensity. Given the isotropy of our samples, and the lamellar character of semicrystalline PEEK, s^2 was selected as the Lorentz factor. The morphological parameters of the lamellar structure of PEEK, the long period (L) and lamellar thickness (L_c), were obtained from $\gamma_1(r)$ using standard approximate relationships[39]

$$\phi_{c,\mathrm{lin}}(1 - \phi_{c,\mathrm{lin}})L = r_0 \qquad (7)$$

$$L_c = \phi_{c,\mathrm{lin}} L \qquad (8)$$

In eqs 7 and 8 $\phi_{c,\mathrm{lin}}$ stands for linear crystallinity, L is determined from the location of the first subsidiary maximum of $\gamma_1(r)$, and r_0 is the first intercept of the tangent to the linear part of the correlation function in the self-correlation triangle with the abscissa ($\gamma_1(r) = 0$). In most cases, eq 7 provides two values for the linear crystallinity, $\phi_{c,\mathrm{lin}}$; we selected the smaller one as the valid one, in agreement with arguments presented elsewhere.[14,40−42] It should be realized, however, that the SAXS model implicit in eqs 7 and 8 is but a very coarse approximation of a complex microstructure; therefore, parameters such as L_c (and to a lesser extent L) should not be considered too strictly.

Wide-angle X-ray scattering (WAXS) patterns were collected in transmission between 13.5° and 26.4° (2θ) in an evacuated Kratky camera with a reduced sample-to-detector distance. Given the selected geometry, our position-sensitive proportional counter had an effective angular step of 0.033°. The diffractograms were absorption-corrected and then numerically corrected to remove the parallax error of the detector[43] and the effects due to the finite widths of the sample and of the detector window. We checked that the corrected data were identical to data acquired with a classical diffractometer working in the Bragg−Brentano reflection geometry. Using our modified Kratky setup for collecting the WAXS allowed to decrease collection times by a factor of 100 as compared to our classical diffractometer, while at the same time allowing to decrease sample size. The desmeared patterns were fitted to a linear superposition of Pearsons distributions of type VII and third order[44] representing the crystalline reflections, plus an empirical function representing the amorphous halo. A crystallinity index ($A_{c,\mathrm{WAXS}}$) was obtained by ratioing the area under the crystalline peaks to the total area in the range 2θ

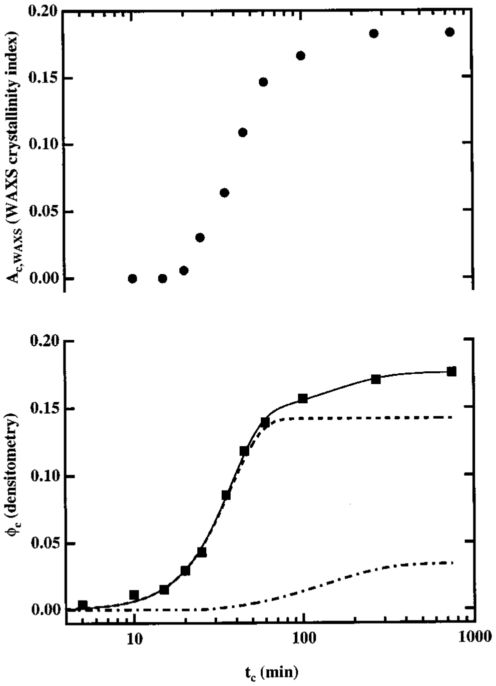

Figure 1. Evolution with crystallization time at 156 °C of the WAXS index of crystallinity of PEEK (determined at RT) (●) and crystallinity obtained from densitometry (RT measurements) (■). The continuous line is the fit of eq 12 to the densitometry data. The dashed line is the crystallinity associated with the first stage, while the dashed/dotted line corresponds to the second stage.

= 13−27°. Only the distance between (110) planes, d_{110}, could be computed with some accuracy, since the extreme broadness and weakness of other reflections prevented an accurate evaluation of other interplanar distances. For some samples, experiments were also performed in reflection with a Siemens D5000 diffractometer fitted with a graphite secondary monochromator. In this case, the average value from transmission and reflection experiments was selected for d_{110}. Accuracies of about 0.005 Å have been estimated for d_{110}.

Atomic Force Microscopy (AFM). AFM topography images of the surfaces of thin PEEK films on mica were obtained in contact mode (constant force) with 0.6 μm thick silicon nitride cantilevers ($k_c \sim 0.3$ N m^{-1}) at room temperature (RT) with an Autoprobe CP (Park Scientific Instruments, Sunnyvale, CA). The appearance of a topographic contrast for the semicrystalline films may be due to the density difference between amorphous and crystalline regions and possibly also to the special edge-on orientation of PEEK lamellae grown in thin films.[45]

Results

Our experiments have been performed at $T_c = 156$ °C, about 10 °C higher than the T_g of pure amorphous PEEK. This low T_c which only slightly exceeds the T_g of the initially amorphous sample presents two experimental advantages. First, one can disregard any thermal degradation of PEEK even after a very long crystallization time, and second, all dynamic effects occurring when heating the sample up to T_c, or cooling it below T_c, can be neglected.[14] Therefore, given the slow crystallization rate of PEEK at this temperature, it is easy to stop the crystallization process after different times, simply by rapidly cooling the sample a few degrees below our T_c. Subsequent analyses can then be performed at RT on samples of increasing crystallinity.

Crystallinity Measurements. Figure 1 presents the WAXS crystallinity index $A_{c,WAXS}$ (RT measurements) and crystallinity (ϕ_c) obtained from densitometry for PEEK crystallized isothermally at 156 °C as a function of crystallization time (t_c). As expected, the crystallinity develops along a typical sigmoidal curve. A short initial induction period is followed by a crystallization, and finally, crystallization dramatically slows down for t_c's larger than 60−100 min. Nevertheless, the transformation does not stop completely at this stage, and some evolution of both $A_{c,WAXS}$ and ϕ_c is still detectable after more than 6 h. The crystallinities determined by both techniques are in reasonable agreement with each other, although an increase of specific weight is already detected for crystallization times comprised between 5 and 15 min, while $A_{c,WAXS}$ does not vary for such short crystallization times.

DSC Results. Figure 2 displays the evolution of the DSC traces of the samples in the glass transition region at different crystallization times. The thermograms show first a specific heat jump associated with the glass transition, followed by an exotherm due to further crystallization during the DSC scan of the originally incompletely crystallized samples. As reported before,[16] the specific heat jump broadens and decreases in amplitude with crystallization time. A displacement of the average location of the glass transition toward higher temperatures is also detected, in agreement with previous reports.[15,16] However, our experimental observations are more complex: together with the broadening, we observe the appearance of two neatly resolved glass transitions for t_c's = 17 and 22 min (Figure 2A), followed by a cold crystallization exotherm (inset of Figure 2A). This is shown more prominently in Figure 2B, where we present the first derivatives of the DSC curves to concentrate the reader's attention on the existence of these two glass transitions. While the first T_g (T_{g1} = 140−143.5 °C) remains in the close proximity of the DSC T_g of the initially amorphous PEEK (139.5 °C), the second T_g (T_{g2}) is located at higher temperatures (147.0−153.0 °C). With the increase of t_c the first glass transition disappears, leaving only the second one. Significant changes are observed in the thermograms even after long crystallization time, consistent with the observations of the previous section. Additionally, the disappearance of the heat capacity jump associated with the first glass transition is paralleled by a strong decrease of residual cold crystallization enthalpy. We thus observed that during the first 22 min of crystallization the latter parameter decreased from 24.6 (fully amorphous sample) to 3.8 J/g (t_c = 22 min), while the former changed from 0.38 to 0.09 J g^{-1} K^{-1} in the same time interval.

Dynamic Mechanical Analysis. To examine in more detail the evolution of the glass transition region, we have undertaken a DMA study. Figure 3A presents the evolution of the dynamical mechanical relaxation of PEEK during cold crystallization at $T_c = 156$ °C. Again, the presence of two glass transitions can be clearly visualized on some of these curves (e.g., t_c = 45 min, shown magnified in Figure 3B). The crystallization times for which two T_g's can be detected are different in DMA and DSC experiments, due to differences in temperature calibration. However, both techniques indicate the coexistence of two glass transitions for intermediate crystallization times. Considering the agreement between DSC and DMA about the existence of two T_g's, we may separate the crystallization process into two stages according to the evolution of the

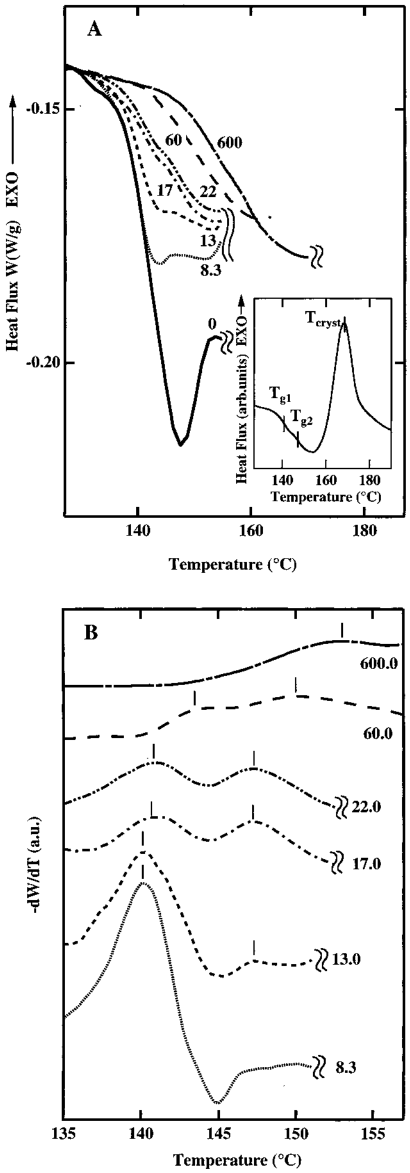

Figure 2. DSC curves (A) and their temperature derivatives (B) corresponding to PEEK samples isothermally crystallized for various times (t_c) at $T_c = 156$ °C and subsequently rescanned in a temperature ramp. The crystallization times in minutes are indicated in the figure for each curve. Heating rate: 10 °C/min. The residual cold crystallization exotherms are masked to facilitate the comparison between the curves. Two glass transitions can be clearly visualized in the thermograms corresponding to $t_c = 17$ and 22 min. A thermogram corresponding to $t_c = 22$ min is enlarged in the inset of (A). It shows two neatly resolved glass transition temperatures, $T_{g1} = 140.9$ °C and $T_{g2} = 147.2$ °C, together with a cold crystallization exotherm having a maximum at $T_{cryst} = 168.1$ °C.

α-relaxations. The first stage is characterized by the progressive disappearance of the α_1 relaxation peak corresponding to the glass transition of the initial amorphous polymer (DMA $T_{g1} \sim 143$ °C). This stage ends after about $t_c = 60-100$ min, when no more traces of the α_1 relaxation can be detected. The second stage corresponds to the development of a new relaxation (α_2) at a temperature $T_{g2} > T_{g1}$. The α_2 relaxation can only be detected by the asymmetric broadening of the α_1 relaxation peak for t_c's lower than 25 min. Then it clearly develops at the expense of the α_1 relaxation, which progressively disappears, for crystallization times between 30 and 60 min. In this time range a clear bimodal relaxation pattern can be evidenced on the DMA curves (Figure 3B). Finally, for t_c's larger than 60–100 min, only the α_2 relaxation remains, slowly shifting with time toward higher temperatures.

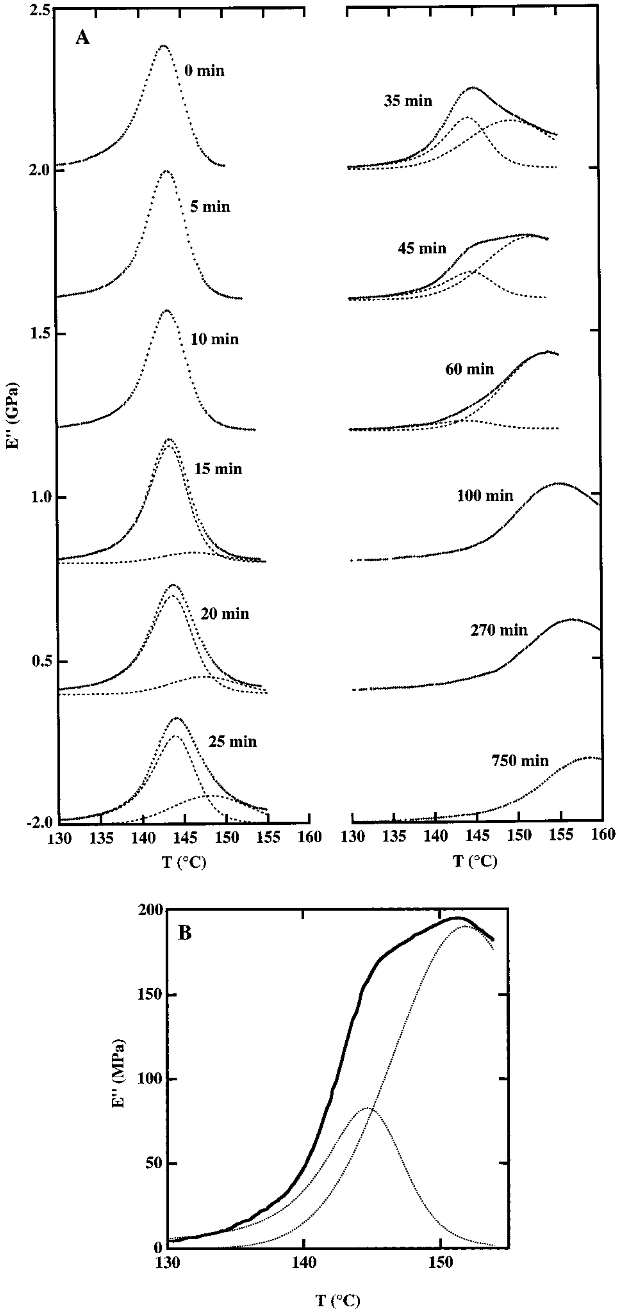

Figure 3. (A) PEEK dynamic mechanical loss modulus (linear scale) versus temperature for samples crystallized for different times at 156 °C. The experimental data (+) have been separated into the sum of two loss peaks (α_1 and α_2). The result of the decomposition is displayed with dashed lines. (B) A DMA trace from (A) corresponding to $t_c = 45$ min that clearly shows the coexistence of α_1 and α_2 relaxations; decomposition into two processes is shown with dashed lines.

X-ray Study. SAXS curves (raw data, together with background corrected and desmeared curves) are presented in Figure 4A,B. The values of intensity are plotted in logarithmic units, and the curves are vertically shifted for clarity. On both corrected and raw curves, we can note the appearance and growth of a broad peak at about 0.008 Å^{-1} corresponding to the formation of the lamellar structure. This peak can

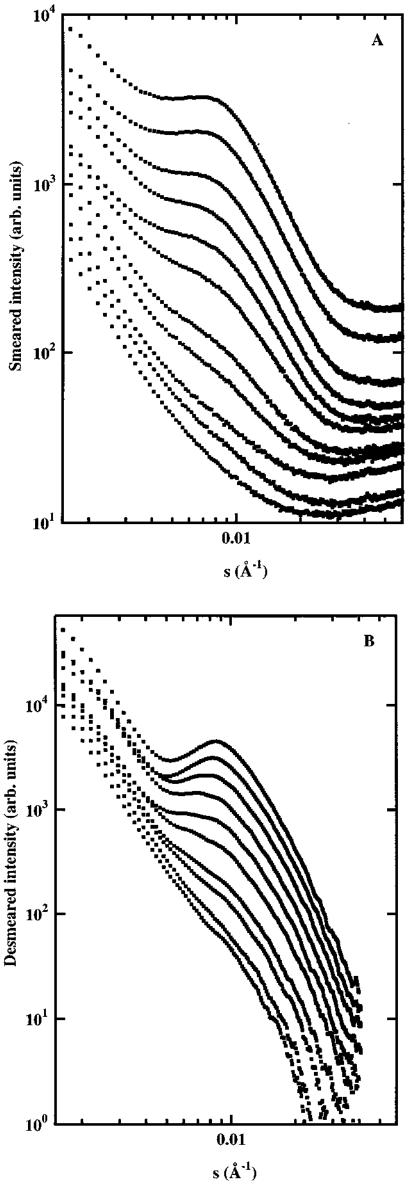

Figure 4. SAXS data obtained for the PEEK samples crystallized at 156 °C: (A) raw data corresponding to 0, 10, 15, 20, 25, 35, 45, 60, 100, 270, and 750 min of PEEK crystallization from bottom to top. The curves are vertically shifted for clarity. (B) Corrected and desmeared data corresponding to the 10, 15, 20, 25, 35, 45, 60, 100, 270, and 750 min of PEEK crystallization from bottom to top. The curves are vertically shifted for clarity.

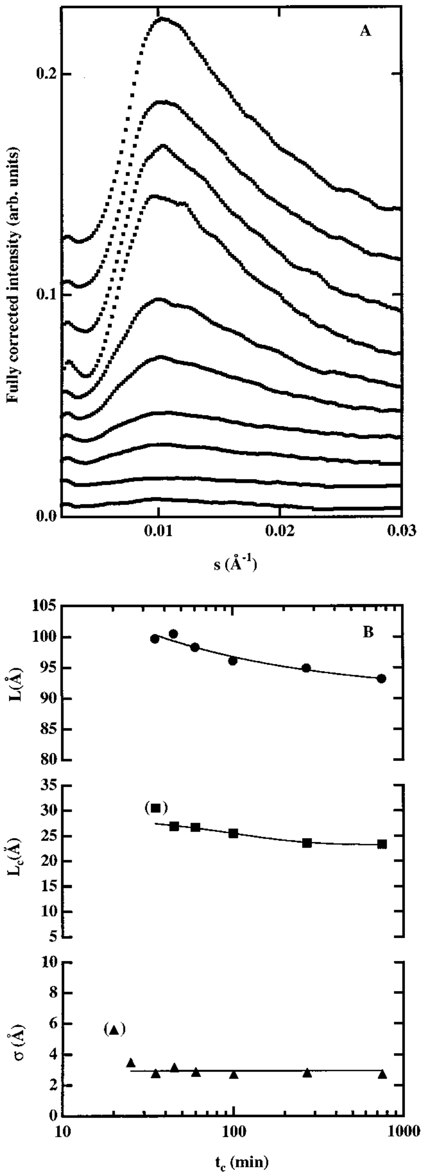

Figure 5. (A) Lorentz-corrected SAXS curves for the PEEK samples crystallized at 156 °C. Data correspond to 10, 15, 20, 25, 35, 45, 60, 100, 270, and 750 min of crystallization from bottom to top. The curves are vertically shifted for clarity. The curves have been corrected for the central scattering for s values below 0.005 Å^{-1}. (B) Long period (●), lamellar thickness (■), and RMS thickness of a density transition layer (▲) for the PEEK samples crystallized at 156 °C.

already be detected after 10 min crystallization time, confirming the observation made by densitometry.

For small scattering vectors (s < 0.005 Å^{-1}), the intensity decreases approximately as s^{-3} for all samples; the same observation was made previously[42] on the SAXS of PEEK and PEEK/poly(ether–imide) blends obtained with a synchrotron source of X-rays.

This low-angle central scattering is usually ascribed to impurities present in commercial polymers. The simple scaling law of this scattering allows to easily remove its contribution from the total scattering. After subtraction of the central scattering, the intensities were Lorentz-corrected (Figure 5A). As can be checked in double-logarithmic coordinates, the shape of these curves is approximately constant from the very beginning of crystallization. This indicates that lamellar microstructures grown at the earliest times of the crystallization are basically identical to those grown for the longest crystallization times. A more refined analysis was performed based on the one-dimensional correlation function. The resulting parameters are presented in Figure 5B and Table 1 together with the values of the parameter σ characterizing the width of density transition layers at the crystal surface (see Experimental Section). Note that the correlation functions could only be computed for times larger than ~45 min, when the signal due to the lamellar structure was significantly strong.

As expected from our previous observations, the SAXS morphological parameters vary little during crystallization. This limited variation does not allow to distinguish specific features corresponding to the two stages detected by DMA and DSC. The long period and linear crystallinity decrease slightly with crystallization time.

Table 1. Evolution of Some Morphological Parameters of PEEK with Crystallization Time at 156 °C

t_c (min)	L_c (Å)[a]	L_a (Å)[a]	$\phi_{c,lin}$[b]	d_{110} (Å)[c]	110 HWHM(2θ)[d]
15					
20					
25					
35	(30.5)			4.762	0.41
45	26.9	73.6	0.268	4.754	0.42
60	26.7	71.6	0.272	4.759	0.39
100	25.5	70.6	0.265	4.756	0.43
270	23.6	71.3	0.249	4.748	0.41
750	23.3	69.8	0.250	4.751	0.39

[a] Lamellar thickness and thickness of the amorphous interlamellar regions estimated from the one-dimensional correlation function. [b] Linear crystallinity as obtained from the analysis of the one-dimensional correlation function. [c] Distance between (110) planes in the crystal (average of two different measurements). [d] Half-width at half-maximum of the 110 reflection.

To this variation corresponds a slight decrease of the parameters L_c and L_a traditionally considered as respectively the thickness of crystalline and noncrystalline regions. However, given the simplicity of the model used to analyze the SAXS, one should not consider these parameters as being strictly equal to the thickness of these regions. The width of density transition layers remains constant at a small value all along crystallization.

At the level of the crystal unit cell, practically no variation could be detected in the limits of our experimental resolution. In the WAXS data, the most intense reflection (110) may tend to shift to slightly smaller distances with crystallization time, without any significant variation in the width (HWHM) of this signal (Table 1). However, this effect is of very limited extent, and at any rate, the observed variation of d_{110} is much lower than that reported with increasing crystallization temperature (see for example the work by Hay et al. referenced in ref 35).

AFM Study. The AFM images obtained at different stages of crystallization of thin PEEK films are displayed in Figure 6. While the limited resolution of these images does not allow to obtain information about lamellar-scale structures, they provide valuable insights about the general patterns of the spherulitic growth at such very low crystallization temperature. The growth proceeds via fanning out of an initial sheaflike structure, eventually leading to complete spherulitic development. This behavior is not significantly different from what is reported for much higher crystallization temperatures. The spherulitic radii remain small (about 1.0−1.5 μm), which prevents obtaining meaningful information by optical microscopy.

Discussion

Earliest Times of Crystallization. For t_c's less than or equal to 15 min, a slight densification of the sample is already detected, together with first traces of the broad peak due to lamellar structures in the SAXS. However, no traces of crystallinity could be detected by WAXS for such short times. This is most probably due to the poor quality of the first crystals appearing, giving rise to broad WAXS reflections not separable from the amorphous halo. Alternatively, one could also think that the difference between WAXS, on one hand, and SAXS/densitometry, on the other, could be due to the existence of regular density fluctuations appearing before the actual crystallization of the sample, as recently proposed for PET by Imai and co-workers.[46] However, the similarity in shape and location of the SAXS of the samples whatever their crystallization times (Figure 5A) does not support this hypothesis, as the fluctuations reported by Imai et al.[46] were characterized by wavelengths different from the ones characterizing the lamellar microstructure.

Origin of the Two α-Relaxations Observed during Crystallization. The sample morphology during crystallization is highly heterogeneous, with the coexistence of large amorphous regions and of interlamellar amorphous regions of much smaller size. For semirigid polymers as PEEK, the α-relaxation associated with interlamellar amorphous regions is located at higher temperatures (by 10−20 °C) than the α-relaxation of pure amorphous PEEK.[15,16,32,41] This is ascribed to the decreased mobility of the chains in these regions, due to their tethering to nearby crystal surfaces and possibly also to an increased concentration of entanglements compared to the bulk amorphous sample. Hence, it is most logical to associate the first relaxation (α_1) to the large amorphous regions not yet crystallized either in interspherulitic spaces or in interfibrillar spaces in the spherulitic envelopes and the second relaxation (α_2) to interlamellar regions and to the portions of interfibrillar amorphous regions directly adjacent to the crystals. Similar observations were obtained for PET by others.[12,47]

Crystallization As Seen from the Viewpoint of Amorphous Regions. This assignment provides us with a tool to follow crystallization "in inverted colors", i.e., from the viewpoint of amorphous regions instead as from the usual viewpoint of crystalline regions. Indeed, (a) the progressive disappearance of the α_1 relaxation allows to follow the ongoing engulfing of large amorphous regions by the growing spherulites, and (b) the progressive shift of the α_2 relaxation toward higher temperatures allows to study the continuing constraining of interlamellar and interfibrillar amorphous regions due to the evolution of crystallinity in already-formed lamellar stacks.

To reach this objective, we must be able to separate the relaxation peaks into their two subrelaxations α_1 and α_2. This necessarily introduces some arbitrariness; however, the validity of the procedure can be checked by the consistency of the results. Thus, we decompose the $E''(T)$ curves into the sum of two relaxations (Figure 3):

$$E''(T) = E''_{\alpha 1}(T) + E''_{\alpha 2}(T) \qquad (9)$$

with both $E''_{\alpha 1}$ and $E''_{\alpha 2}$ being described by *empirical* functions of the type

$$f(T) = \frac{a_0 T^p}{[1 + a_1(T - T_0)^2]^m} \qquad (10)$$

This function, a Pearsons function[44] of type VII and order m multiplied by a skewing factor (T^p), was found to represent properly the shape of the loss modulus of the α_1 relaxation of pure amorphous PEEK. Therefore, the same functional dependence with p and m fixed was selected to represent the α_1 relaxation during crystallization. In this expression, a_1 and T_0 were allowed to vary slightly to accommodate minor shifts and a small broadening of the α_1 relaxation during crystallization, and a_0 varied according to the evolution of the strength

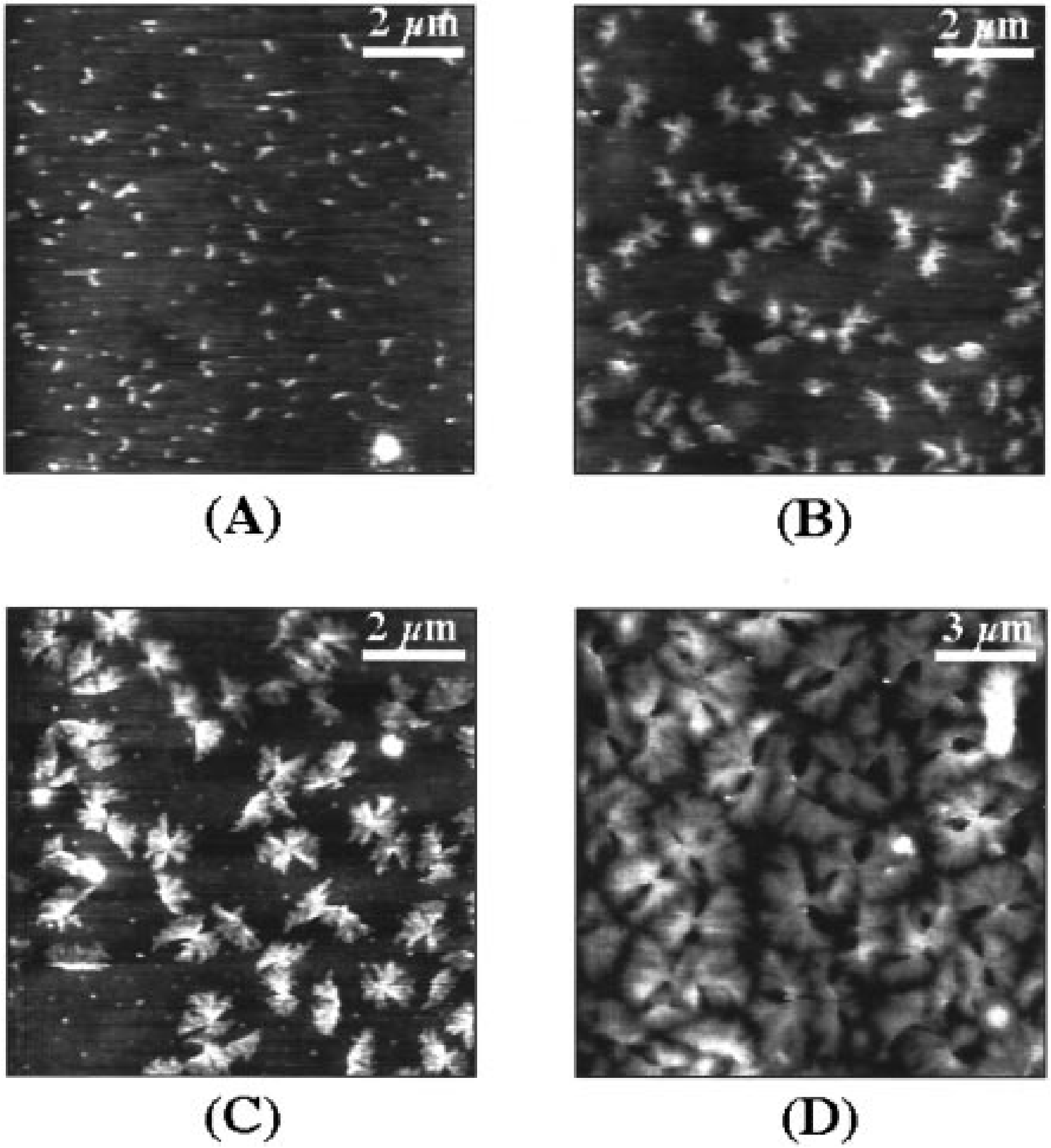

Figure 6. AFM topographical images of PEEK spherulites growing at 156 °C in thin films deposited on mica. Crystallization times (t_c's) are the following: (A) $t_c = 1$ min; (B) $t_c = 4$ min; (C) $t_c = 8$ min; (D) $t_c = 15$ min. The vertical gray scale corresponds to 100 Å.

of the α_1 relaxation. The same functional form could also represent the shape of the loss modulus of the α_2 relaxation of PEEK samples with no trace of α_1 relaxation (e.g., after 750 min of crystallization).

The fits were virtually identical to the data (Figure 3), and the temperature maxima of the two relaxations were identical to the values found by a second-derivative procedure.[48] The evolutions with crystallization time of the temperature maxima of the α_1 and α_2 relaxations are presented in Figure 7A and the evolution of the integral in the temperature domain of the $E''_{\alpha 1}$ loss modulus in Figure 7B. The temperature location of the first relaxation subpeak (α_1) remains approximately constant during crystallization, while its intensity decreases sigmoidally with time. By contrast, the temperature location of the second subrelaxation (α_2) steadily increases with time with a slowing down of this increase after ~100 min. It should be noted that this crystallization time roughly corresponds to the point of isothermal vitrification of the constrained amorphous regions, defined from the condition $T_{g2} = T_c$ (Figure 7A). Vitrification during crystallization results in a strong slowing down of the molecular mobility and, as a consequence, gives rise to a dramatic retardation of the overall crystallization kinetics. This effect was analyzed in some detail elsewhere.[32] Hence, while large amorphous regions (related to the α_1 relaxation) are simply progressively eaten away by the growing spherulites, interlamellar amorphous regions belonging to already grown lamellar stacks, and the portions of interfibrillar regions directly adjacent to the stacks, are increasingly constrained with time. This indicates that at least two crystallization mechanisms must be acting during crystallization: the first related to the usual spherulitic growth and the second one occurring in and at the border of, already formed, lamellar stacks. Accordingly,

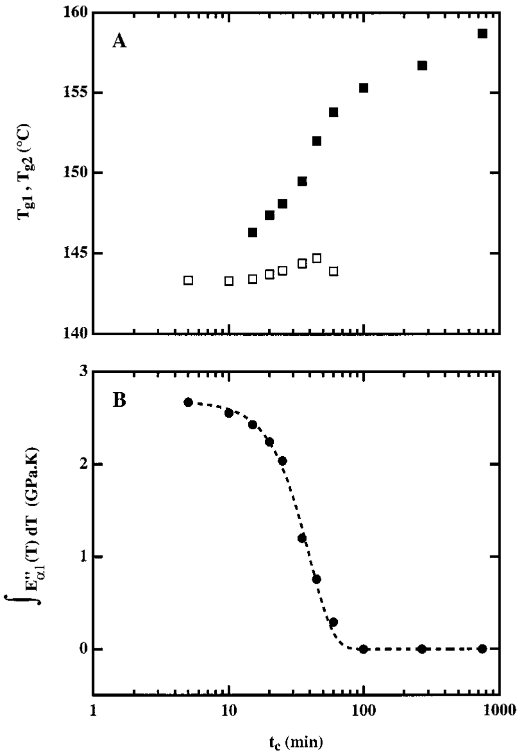

Figure 7. (A) Evolution with crystallization time at 156 °C of the temperature locations of the two maxima of the PEEK loss modulus (□, T_{g1}; ■, T_{g2}). (B) Evolution with crystallization time at 156 °C of the integral of the $E''_{\alpha 1}$ loss modulus of PEEK in the temperature domain (α_1 relaxation only). This integral is proportional to the amount of unconstrained bulk amorphous phase progressively engulfed by the growing crystals, $\phi_{\alpha 1}(t)$. The dashed line is a fit of the simple Avrami equation to the data.

one expects to observe two stages in the overall crystallization kinetics of PEEK as disclosed by other methods. We will soon come back to this point.

Since the shape of the α_1 relaxation is practically invariant during crystallization, and since the loss modulus E'' is a measure of the energy lost per cycle of sinusoidal deformation, the integral in the temperature domain of $E''_{\alpha 1}$ can be considered as proportional to the remaining amount of unconstrained bulk amorphous phase at a given time t, $\phi_{\alpha 1}(t)$. $\phi_{\alpha 1}(t)$ represents thus the complement to the volume fraction occupied by crystalline stacks at time t. As such, it is insensitive to secondary mechanisms acting inside or at the borders of lamellar stacks, like stack or crystal thickening, crystal perfection, etc. If we assume that the growth rates of lamellar stacks are constant all along crystallization, which seems reasonable given the near invariancy of their structural characteristics revealed by SAXS (see section 5 for more details), one expects $\phi_{\alpha 1}(t)$ to follow a simple Avrami-like equation:

$$\phi_{\alpha 1}(t) = \phi_{\alpha 0}(t) \exp(-K_1 t^{n_1}) \tag{11}$$

where the value of n_1 is dependent upon the geometry of the growth, and K_1 is a rate constant. The fit of $\phi_{\alpha 1}(t)$ to eq 11 is shown in Figure 7. Parameters are presented in Table 2. The fit is satisfactory, with no deviations at short or long crystallization times. The value of n_1, lower than 3, probably results from the complex variation of the growth shape of the spherulites with time, in agreement with the microscopical observations of Figure 6.

Crystallization As Seen from the Viewpoint of Crystalline Regions. A crucial step in our reasoning is the confrontation of the results obtained from the evolution of amorphous regions with the results obtained by techniques directly sensitive to crystallinity, e.g., WAXS, densitometry, and SAXS. According to the results of the previous section, one expects a two-stage crystallization mechanism for the sample. Thus, any property $P(t)$ linearly dependent on the overall crystallinity can be expressed as follows:

$$P(t) = P_0 + P_1(t) + P_2(t) = P_0 + W_1(1 - \exp(-K_1 t^{n_1})) + W_2(1 - \exp(-K_2(t - t_0)^{n_2})) \tag{12}$$

where W_1 and W_2 represent the relative weight of both stages in the overall crystallization and P_0 is the value of the property at time zero (pure amorphous sample). By writing eq 12, we only follow a well-established line of modeling, which has been empirically developed in order to remedy for the deficiencies of the simple Avrami equation in representing the actual crystallization of polymers.[25,27,29] The important difference with this tradition is, in our case, that we have specific extra information as to the origin of these two stages. We have thus fit eq 12 to the densitometry data. Results are reported in Table 2, and the fit is shown in Figure 1. A very good agreement is observed between the n_1 and K_1 values found from fits to the DMA and densitometry data, respectively. The ratio of the first stage to the overall crystallization is about 80%, which seems reasonable, since it agrees with results previously reported by others on the isothermal and anisothermal crystallization of PET[26] and PEEK.[29,49] The parameters of the second process K_2 and the time offset (t_0), however, cannot be evaluated with sufficient precision from the fit, due to the smaller number of experimental points affected by the second process.

The agreement between our DMA and densitometry analysis is rewarding and supports a posteriori the validity of our decomposition of the crystallization process into two stages. We now may sum up our observations:

(a) The crystallization of PEEK follows a two-step process.

(b) The first step corresponds to the outward growth of the spherulites and their infilling by new lamellar stacks. This stage can be described by a single Avrami equation and results in the complete disappearance of any large amorphous (unconstrained) regions. In our case, it stops after about 60 min crystallization time.

(c) The second stage occurs in already-grown lamellar stacks and in the portions of interfibrillar spaces adjacent to the lamellar stacks. It represents about 20% of the overall final crystallinity. It results in an increasing constraining of these amorphous regions and leads to the vitrification of these regions followed by a dramatic slowing down of the transformation kinetics. This stage begins already during the outward spherulitic growth and extends for very long times.

A Lamellar-Scale Picture of Crystallization. Lamellar-scale information is provided by SAXS, WAXS, and the evolution of the α_2 relaxation (which originates from interlamellar amorphous regions and the portions of interfibrillar spaces adjacent to the lamellar stacks). Missing in this work is lamellar-scale microscopy, i.e., transmission electron microscopy; however, previous works by Lovinger et al.[50] have already illustrated the

Table 2. Fit of the Single and Double Parallel Avrami Models to the Crystallization Data

origin of the data	K_1^{1/n_1} (min^{-1})	n_1	K_2^{1/n_2}(min^{-1})	n_2	$W_1/(W_1 + W_2)$	t_0 (min)
DMA, $\phi_{\alpha 1}(t)$	$2.5 \times 10^{-2} \pm 3 \times 10^{-3}$	2.46 ± 0.09				
densitometry	$2.7 \times 10^{-2} \pm 3 \times 10^{-3}$	2.34 ± 0.08	7.7×10^{-3} [a]	1.19 ± 0.5	0.81 ± 0.07	24.6[a]

[a] The precision on parameters K_2 and t_0 obtained from the double Avrami fit is very low due to the small number of significant points.

main morphological pictures of PEEK spherulites at the nanometer scale, albeit for samples crystallized at higher temperatures.

A striking observation is that the long period decreases by less than 10% over the whole crystallization (Table 1). This obviously rules out a crystallization mechanism by which lamellae would grow randomly over space. In such a case, the progressive infilling of dilute lamellar stacks by new lamellae (random lamellar insertion) would have led to a large decrease of L with time. Instead, the near constancy of L over time indicates that the growth proceeds by entire stacks, i.e., by bundles of a few lamellae growing simultaneously. We have already pointed out this intrinsic tendency of lamellae to grow closely together from studies on PEEK/PEI blends;[42] in addition, electron micrographs of Lovinger et al.[45,50] support this conclusion.

Given the limited variation observed by SAXS and the probable complexity of the analyzed system, caution should be exercised when interpreting these data. Simple concepts such as the equivalence between the long period and the average distance between lamellae in stacks are no more strictly valid. For instance, we show in the Appendix that the progressive thickening of lamellar stacks by the addition of new lamellae at their border may result in a decrease of long period by as much as 17%, while the average distance between lamellae and lamellar thickness remain constant. Others have also suggested that variation of L may originate from other mechanisms, e.g., flattening of initially corrugated lamellae.[51] Accordingly, in this study, we did not attempt to analyze in fine detail the SAXS results; however, we simply point out that the observed variation of the SAXS parameters may be explained simply by the progressive thickening of lamellar stacks and does not require any consideration of lamellar insertion mechanisms. At this stage, we are in a position to reconcile the structural data obtained from the X-ray study with the data on crystallinity and relaxation provided by other techniques, to propose a consistent lamellar-scale model of the overall crystallization. We assume that, during the first stage, only relatively thin lamellar stacks containing 3−5 lamellae are growing. Further growing of these stacks by the parallel addition of new lamellae will then contribute to decrease the parameter L; simultaneously, the formation of these new lamellae will constrain further small amorphous regions sandwiched between two neighboring stacks which may explain in part the progressive shift of T_{g2}. Other mechanisms such as crystal perfection and thickening will also contribute to increase T_{g2}. In this context, it should be noted that PEEK crystals are strongly microfragmented.[50] A limited increase of the lateral coherence length of the crystals by the progressive “healing” of defective regions connecting crystal fragments is thus possible and would not be detected given our experimental resolution. Thus, this mechanism could efficiently contribute to the further constraining of the amorphous interlamellar regions.[11,52]

These observations and conclusions are clearly not in accordance with some previous thoughts about PEEK crystallization, while they are in agreement with some other observations. These discrepancies are partly due to the fact that most authors did not consider crystallization at such large undercoolings.

(1) Our experiments show that low-temperature crystallization does not proceed by the progressive insertion of new lamellae in previously formed lamellar stacks, contrary to what is sometimes postulated for high-temperature crystallization.[53] Growth in tight lamellar bundles seems to be more appropriate in our case. This mechanism is also more compatible with electron microscopy observations on the crystallization of other polymers (PS, PE, etc.) that do not provide support for random lamellar insertion processes.[54,55]

(2) Our experiments indicate that no large regions remain uncrystallized in the sample at the end of the cold crystallization process; this is different from what some authors have postulated for high-temperature crystallization,[56] although this hypothesis was challenged by others.[40−42]

(3) The complex crystallization kinetics of PEEK probably results *in part* from crystal growth in amorphous regions of restricted size. This was postulated a long time ago on the basis of DSC crystallization studies.[27] However, there are no indications that the later formed crystals are significantly different from the first crystals growing in the free melt, apart from their growth rate.

(4) The progressive disappearance of the α_1 relaxation and its replacement by the α_2 relaxation pertaining to constrained regions confirm that the relaxation dynamics of PEEK between crystals is much different from bulk amorphous PEEK. Consequently, it is possible to obtain information on the crystallization process simply by following the evolution of both relaxations.

Conclusion

Combining techniques assessing the morphology, crystallinity, and properties of crystals (AFM, WAXS, SAXS, densitometry), together with techniques probing the relaxation behavior of amorphous regions (DSC, DMA), we have studied the cold crystallization of PEEK at low temperature. The two sets of data are consistent and show that the crystallization occurs in a two-stage process. The first stage corresponds to the classical picture of nucleating, growing, and finally impinging entities. During this stage the progressive disappearance of the first glass transition (T_{g1}) or loss modulus peak (α_1 relaxation) associated with free amorphous regions can be detected on the DSC and DMA curves. In a second stage a new glass transition (T_{g2}) or new loss modulus peak appears a few degrees higher (α_2 relaxation) and develops at the expense of α_1 relaxation. Other mechanisms then set in, as soon as free amorphous regions have locally disappeared. These mechanisms dominate crystallization in its second stage, thereby giving rise to a complex crystallization kinetics.

Although many different mechanisms could be reconciled with our data, we have shown that the consideration of a simple mechanism of stack thickening, i.e., the progressive addition of new lamellae at the borders of a previously formed stack, could explain the observed variation of a long period detected during crystallization. In addition, this stack thickening occurring by lamellar growth on the borders of already existing stacks can also account for the increase of crystallinity and part of the progressive shift of the α_2 relaxation toward higher temperatures during the second stage. Miscellaneous perfection mechanisms may also play a role in the increase of T_{g2} as time proceeds. Importantly, the crystals growing during this second stage are not structurally significantly different from the previous ones, as indicated by X-ray scattering experiments. The resulting shift of T_{g2} leads to the vitrification of constrained amorphous regions, further slowing down the kinetics of transformation at this stage. The material then sets into a frozen state and is capable of further crystallization and reorganization upon subsequent heating, as shown elsewhere.[14,32,33,40] The formation of the semicrystalline structure thus results from a complex interplay between the simultaneous evolution of crystalline and amorphous regions and should not be considered as a simple crystallization process.

Acknowledgment. Partial financial support of this work by the Belgian National Fund for Scientific Research (FNRS) is gratefully acknowledged. We also appreciate partial financing of this work in the frame of a “mécénat Sandoz”. We thank Mr. D. Pattijn and Mr. K. Schaap (TA Instruments, Gent) for the help in performing DSC measurements.

Appendix

Simulation of the SAXS Intensity Diffracted by a Finite Lamellar Stack According to the General One-Dimensional Paracrystalline Model of Hosemann. The objective of this simulation is to evaluate the possible variation of structural parameters L and L_c (obtained from a simple analysis of the one-dimensional correlation function) as a function of the number of lamellae (N) in a stack. In this model, the thickness of crystals and amorphous interlayers is represented by independent distribution functions whose Fourier transforms are denoted below by F_c and F_a, respectively. By extending the reasoning presented in ref 57, it can be shown that the intensity scattered from a stack containing N lamellae is given by

$$I_N(s) = \frac{N(\rho_c - \bar{\rho})^2}{2\pi^2 s^2}(1 + R_\rho)^2 \mathrm{Re}\left\{\frac{(1 - F_a)(1 - F_c)}{1 - F_a F_c}\right\} + \frac{(\rho_c - \bar{\rho})^2}{2\pi^2 s^2}\mathrm{Re}\left\{\frac{1 - (F_a F_c)^N}{(1 - F_a F_c)^2}[F_a(1 - F_c)^2 + R_\rho^2 F_c(1 - F_a)^2 - R_\rho F_a F_c(1 - F_a)(1 - F_c)] - R_\rho \frac{(1 - F_a{}^*)(1 - F_c{}^*)(1 - (F_a{}^* F_c{}^*)^N)}{(1 - F_a{}^* F_c{}^*)^2}\right\} \quad (13)$$

where $\bar{\rho}$, ρ_c, and R_ρ are the average electron density of the surroundings of the stack, the electron density of the crystalline regions, and the ratio $(\bar{\rho} - \rho_a)/(\rho_c - \bar{\rho})$, respectively; $F_c{}^*$ and $F_a{}^*$ are the complex conjugates of F_c and F_a. Equation 13 presents a sum of four terms where the first one describes the scattering from an infinite stack, and the others are due to finite stack-size effects. To account for sigmoidal-gradient density transition layers, the result of (14) should be multiplied by $\exp(-4\pi^2 s^2 \sigma^2)$.[37]

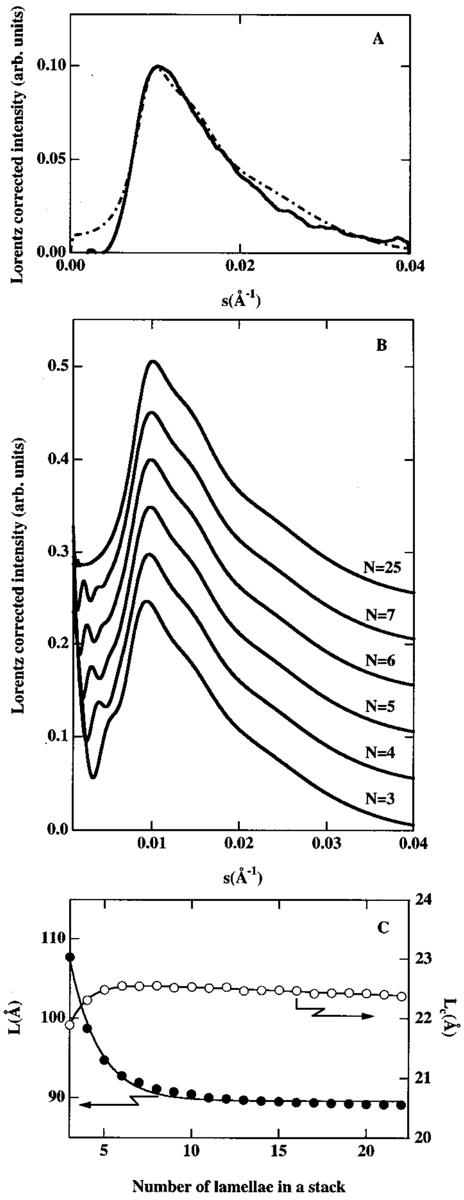

Figure 8. (A) Lorentz-corrected SAXS curves corresponding to the PEEK sample crystallized for 750 min at 156 °C (solid line) together with its approximation by eq 13 (dashed line). The experimental curve has been corrected for the central scattering for **s** values below 0.005 Å^{-1}. (B) Lorentz-corrected SAXS curves calculated in accordance with the general one-dimensional paracrystalline model of Hosemann (eq 13). The number of lamellae in a stack (N) is indicated in the figure for each curve. (C) Structural parameters L and L_c obtained from a simple analysis of the one-dimensional correlation function of the simulated SAXS curves.

To perform simulations, we first fitted eq 13 to the SAXS data of one particular sample (PEEK crystallized for 750 min at 156 °C). We assumed combinations of Gaussian distribution functions for both crystalline and amorphous regions. We observed that the distribution of crystalline regions resulting from the fit was very narrow and symmetrical. By contrast, a broad and asymmetric distribution of thicknesses was found necessary for amorphous regions. Some discrepancies between the experimental and fitted curves are still observed but were not considered as important given our goals (Figure 8A).

The structural parameters found from the fit were then fixed, and N was allowed to vary between 3 and infinity. The corresponding Lorentz-corrected SAXS curves together with L and L_c evaluated from the corresponding one-dimensional correlation functions are shown in Figure 8B,C. We can see that L decreases at small N and remains constant thereafter, while L_c is almost independent of N. Characteristic ripples in the Lorentz-corrected curves visible at very small values of N are related to the stack size and would not show up into actual scattering curves due to convolution and resolution effects.

References and Notes

(1) Mandelkern, L. *Crystallization of Polymers*; McGraw-Hill Book Company: New York, 1964.
(2) Wunderlich, B. *Macromolecular Physics*; Academic Press: New York, 1976; Vol. 2.
(3) Mandelkern, L. *Chemtracks: Macromol. Chem.* **1992**, *3*, 347.
(4) Kumar, S. K.; Yoon, D. Y. *Macromolecules* **1991**, *24*, 5414.
(5) Mandelkern, L. *Acc. Chem. Res.* **1990**, *23*, 80.
(6) Guenet, J.-M.; Picot, C. *Macromolecules* **1981**, *14*, 309.
(7) Mansfield, M. L. *Macromolecules* **1987**, *20*, 1384.
(8) Robelin-Souffaché, E.; Rault, J. *Macromolecules* **1989**, *22*, 3581.
(9) Zachmann, H. G. *Kolloid Z. Z. Polym.* **1967**, *216*, 180.
(10) Fischer, E. W. *Kolloid Z. Z. Polym.* **1967**, *218*, 97.
(11) Waddon, A. J.; Keller, A.; Blundell, D. J. *Polymer* **1992**, *33*, 27.
(12) Vigier, G.; Tatibouet, J.; Benatmane, A.; Vassoille, R. *Colloid Polym. Sci.* **1992**, *270*, 1182.
(13) Vigier, G.; Tatibouet, J. *Polymer* **1993**, *34*, 4257.
(14) Jonas, A. M.; Russell, T. P.; Yoon, D. Y. *Macromolecules* **1995**, *28*, 8491.
(15) Jonas, A.; Legras, R. *Macromolecules* **1993**, *26*, 4489.
(16) Cheng, S. Z. D.; Cao, M. Y.; Wunderlich, B. *Macromolecules* **1986**, *19*, 1868.
(17) Krishnaswami, R. K.; Kalika, D. S. *Polymer* **1994**, *35*, 1157.
(18) Kalika, D. S.; Krishnaswami, R. K. *Macromolecules* **1993**, *26*, 4252.
(19) Cebe, P.; Huo, P. P. *Thermochim. Acta* **1994**, *238*, 229.
(20) David, L.; Etienne, S. *Macromolecules* **1993**, *26*, 4489.
(21) Fulchiron, R.; Gauthier, C.; Vigier, G. *Acta Polym.* **1993**, *44*, 313.
(22) David, L.; Etienne, S. *Macromolecules* **1992**, *25*, 4302.
(23) Huo, P.; Cebe, P. *Macromolecules* **1992**, *25*, 902.
(24) Avrami, J. M. *J. Chem. Phys.* **1939**, *7*, 1103.
(25) Price, F. P. *J. Polym. Sci., Part A* **1965**, *3*, 3079.
(26) Ravindranath, K.; Jog, J. P. *J. Appl. Polym. Sci.* **1993**, *49*, 1395.
(27) Cebe, P.; Hong, S.-D. *Polymer* **1986**, *27*, 1183.
(28) Aggarwal, S. L.; Marker, L.; Kollar, W. L.; Geroch, R. *J. Polym. Sci.* **1966**, *4*, 715.
(29) Cruz-Pinto, J. J. C.; Martins, J. A.; Oliveira, M. J. *Colloid. Polym. Sci.* **1994**, *272*, 16.
(30) Ivanov, D. A.; Jonas, A.; Legras, L. *Bull. Am. Phys. Soc.* **1996**, *41*, 395.
(31) Ivanov, D. A.; Jonas, A. *Bull. Am. Phys. Soc.* **1996**, *41*, 395.
(32) Ivanov, D. A.; Jonas, A. M. *J. Polym. Sci., Part B* **1998**, *36*, 919.
(33) Ivanov, D. A.; Jonas, A. M. *Macromolecules* **1998**, *31*, 4546.
(34) Hemmeinger, W. F.; Sarge, S. M. *J. Therm. Anal.* **1991**, *37*, 1455.
(35) The crystal density of PEEK is dependent on crystallization conditions and can vary between 1.3665 and 1.4109 g cm^{-3} (Hay, J. N.; Langford, J. I.; Lloyd, J. R. *Polymer* **1989**, *30*, 489). The value selected in this paper is close to the average value proposed in: Jonas, A.; Legras, R. In Kausch, H. H., Ed.; *Advanced Thermoplastics and their Composites*; Carl Hanser Verlag: Munich, 1992; p 83.
(36) Ruland, W. *Colloid. Polym. Sci.* **1977**, *255*, 417.
(37) Koberstein, J. T.; Morra, B.; Stein, R. S. *J. Appl. Crystallogr.* **1980**, *13*, 34.
(38) Glatter, O. *J. Appl. Crystallogr.* **1974**, *7*, 147.
(39) Strobl, G. R.; Schneider, M. *J. Polym. Sci., Part B* **1980**, *18*, 1343.
(40) Fougnies, C.; Damman, P.; Dosière, M.; Koch, M. H. *Macromolecules* **1997**, *30*, 1392.
(41) Kalika, D. S.; Gibson, D. G.; Quiram, D. J.; Register, R. A. *J. Polym. Sci., Part B* **1998**, *36*, 65.
(42) Jonas A. M.; Ivanov, D. A.; Yoon, D. Y. *Macromolecules* **1998** *31*, 5352.
(43) Glatter, O.; Kratky, O. *Small Angle X-ray Scattering*; Academic Press: London, 1982.
(44) Veeraraghavan, V. G.; Rubin, H.; Winchell, P. G. *J. Appl. Crystallogr.* **1977**, *10*, 66.
(45) Lovinger, A. J.; Davis, D. D. *J. Appl. Phys.* **1985**, *58*, 2843.
(46) Imai, M.; Kaji, K.; Kanaya, T. *Macromolecules* **1994**, *27*, 7103.
(47) Fukao, K.; Miyamoto, Y. *Prog. Theor. Phys. Suppl.* **1997**, *126*, 219.
(48) Maddams, W. F. *Appl. Spectrosc.* **1980**, *34*, 245.
(49) Cebe, P. *Polym. Eng. Sci.* **1988**, *28*, 1192.
(50) Lovinger, A. J.; Davis, D. D. *Macromolecules* **1986**, *19*, 1861.
(51) Elsner, G.; Zachmann, H. G.; Milch, J. R. *Makromol. Chem.* **1981**, *182*, 657.
(52) Jonas, A.; Legras, R. In Dosière, M., Ed.; *Crystallization of Polymers*; *NATO ASI Ser. C* **1993**, *405*, 619.
(53) Hsiao, B. S.; Gardner, K. H.; Wu, D. Q.; Chu, B. *Polymer* **1993**, *34*, 3986.
(54) Bassett, D. C. *CRC Crit. Rev. Solid State Mater. Sci.* **1984**, *12*, 97.
(55) Vaughan, A. S. *Polymer* **1992**, *33*, 2513.
(56) Hsiao, B. S.; Sauer, B. B.; Verma, R. K.; Zachmann, H. G.; Seifert, S.; Chu, B.; Harney, P. *Macromolecules* **1995**, *28*, 6931.
(57) Hosemann, R.; Bagchi, S. N. *Direct Analysis of Diffraction by Matter*; North-Holland: Amsterdam, 1962.

MA981220O